

Upscaling permeability in anisotropic volcanic systems

Jamie I. Farquharson^{a,b,*}, Fabian B. Wadsworth^c



^aDepartment of Marine Geology and Geophysics, Rosenstiel School of Marine and Atmospheric Sciences, University of Miami, 4600 Rickenbacker Causeway, Miami, FL 33149-1031, USA

^bGéophysique Expérimentale, Institut de Physique de Globe de Strasbourg (UMR 7516 CNRS, Université de Strasbourg/EOST), 5 rue René Descartes, Strasbourg cedex 67084, France

^cDepartment of Earth Sciences, Durham University, Science Labs, Durham DH1 3LE, UK

ARTICLE INFO

Article history:

Received 11 January 2018

Received in revised form 22 August 2018

Accepted 7 September 2018

Available online 14 September 2018

Keywords:

Fluid flow

Anisotropy

Soufrière Hills Volcano

Volcán de Colima

Volcano modelling

Upscaling

ABSTRACT

Permeability is an important input to models of shallow magma ascent. It is a property that can exhibit anisotropy in volcanic magmas, rocks and edifices. Here we show that some important features of permeability anisotropy can be captured by a simple approach. The permeability of a layered medium can be described by a function that takes into account the angle between the direction in which pressure gradient acts, and the layering orientation. In the end-member case of flow parallel or perpendicular to the layering, the permeability of the whole system reduces to the arithmetic or harmonic means of the permeabilities of the constituent units, respectively. This implies that laboratory-scale measurements on homogeneous constituent layers can be upscaled to an effective permeability of a larger, multi-layered unit or edifice, including fractured systems. We outline the theoretical underpinning to these formulations, and provide experimental permeability data measured on anisotropic volcanic materials in order to validate this result. We show that this result implies that permeability parallel to layering or bedding must always be higher than that measured perpendicular to layering. Moreover, we emphasise that the choice of averaging method used to upscale permeability data on individual rock samples has important consequences for the validity of the derived values. We anticipate that these points will help move towards more realistic models of pressure evolution behaviour in volcanoes, and increase the utility of laboratory-derived data for volcano-scale modelling.

© 2018 Elsevier B.V. All rights reserved.

1. Introduction

It is well established that permeability—the capacity for fluid flow through a porous or granular medium—is a fundamentally important property influencing fluid pressure in volcanic systems (e.g. Eichelberger et al., 1986; Melnik et al., 2005). Over the last three decades, volcanic rock permeability has become an increasingly prevalent parameter in the discussion of mechanisms for volcano outgassing and—in turn—eruption dynamics. Since the work of Eichelberger et al. (1986), numerous studies have examined the permeability of natural and synthetic volcanic materials representing a wide variety of volcanic systems (e.g. Westrich and Eichelberger, 1994; Klug and Cashman, 1996; Mueller et al., 2005; Degruyter et al., 2010; Kolzenburg et al., 2012; Ashwell et al., 2015; Heap et al., 2015; Farquharson et al., 2015, 2016; Wadsworth et al., 2016; Kushnir et al., 2016, 2017a, amongst many others).

Measurements of the Darcian permeability on centimetric-scale samples—whilst useful in their own right—do not necessarily reflect the fluid flow characteristics of a volcanic edifice, geothermal reservoir, or any other large system under investigation. Indeed, the ability to “upscale” rock physical properties merits consideration in any case where the scale of measurement is smaller than that at which the data are applied. For certain constitutive physical properties, upscaling is somewhat trivial. For example, the average porosity ϕ of a system is simply the mean value of each of the porosities of the constituent units, independent of any direction of interest, which is to say that porosity is a scalar property. However many rock physical properties are not scalars, and weighted averaging laws that depend on the direction of interest become necessary in order to incorporate measured data into system-scale models (e.g. Tidwell, 1996).

The ability to upscale permeability from the scale of laboratory specimens to that of an outcrop, conduit, or volcanic edifice has been a feature of recent research efforts (e.g. Heap and Kennedy, 2016; Farquharson et al., 2016, 2017b; Lamur et al., 2017) which have sought to explain the influence of heterogeneities (such as fractures) on the permeability of magma or edifice rock. The inclusion of edifice or magma permeability as a variable parameter has helped

* Corresponding author at: Department of Marine Geology and Geophysics, Rosenstiel School of Marine and Atmospheric Sciences, University of Miami, 4600 Rickenbacker Causeway, Miami, FL 33149-1031, USA.

E-mail address: james.farquharson@rsmas.miami.edu (J.I. Farquharson).

move towards more realistic gas evolution models for volcanic systems (Jaupart, 1998; Collombet, 2009; Collinson and Neuberg, 2012; Chevalier et al., 2017). The increased use of laboratory data in numerical models (e.g. Chevalier et al., 2017) is valuable; nevertheless, it is important to note that as this trend continues, the choice of averaging method is ever more critical for accurately transferring data between scales (e.g. Tidwell, 1996). Indeed, this is commonly acknowledged in studies associated with hydrocarbon exploration and research (e.g. Cardwell et al., 1945; Christie et al., 2001; Pickup et al., 2005), and sedimentology or studies of sedimentary basin evolution (e.g. Gingras et al., 2012; Jensen et al., 1994).

One of the primary complexities involved in upscaling permeability is the existence of significant anisotropy in the media under investigation. Numerical modelling of groundwater flow in a volcanic edifice by Hurwitz et al. (2003) highlights that very slight changes in permeability—and in particular, anisotropy thereof—can result in significant changes in the elevation of the water table within a volcanic edifice, as well as its internal thermal structure and phase distribution. In turn this has consequences for the likelihood of slope failure, phreatic eruptions, lahar generation, and other volcanic hazards, as well as the potential of a volcanic region in terms of geothermal energy extraction and epithermal mineralisation. Anisotropy exists in volcanic systems at many scales, and examples of the phenomenon are as myriad as its causes. Magma properties evolve in space and time, resulting in spatially variable crystal content (e.g. Caricchi et al., 2007; Vona et al., 2011; Chevrel et al., 2013, 2015), porosity (e.g. Bagdassarov and Dingwell, 1992; Farquharson et al., 2015, 2016; Wadsworth et al., 2017), and geochemistry (e.g. Giordano et al., 2008). Magma is also buffeted by variations in in-situ stress conditions and strain rate partitioning (e.g. Papale, 1999; Gonnermann and Manga, 2003; Caricchi et al., 2007) within the volcanic conduit—processes that continue during extrusion and emplacement (e.g. Smith et al., 2001; Cashman et al., 2008).

During the ascent, evolution, and eventual emplacement of magma, a host of heterogeneities can form and grow due to mechanisms such as tensile fracturing, partial or complete healing of fractures, cavitation, or inhomogeneous bubble expansion and collapse. Ultimately, this can result in anisotropy on the micro-scale (Farquharson et al., 2016). Fig. 1A shows an example of this, where magmatic processes (fracturing and partial sintering) have resulted in planar heterogeneities in an andesitic lava.

Syn- and post-emplacement processes may also contribute significantly to the development of anisotropy in volcanic systems. Fall deposits often exhibit well-defined bedding (e.g. Wilson and Hildreth, 1997), with individual laminae occurring on the centimetric-scale and smaller. Fig. 1B shows finely bedded ash from Whakaari, New Zealand. In this example, discrete laminae tend be less than 10 mm in thickness. Pyroclastic flow phenomena may often sediment layered deposits as a result of sequential or coeval deposition in the tractional regime, or due to fluidisation, elutriation, and sedimentation processes occurring during and after their emplacement (e.g. Wilson and Hildreth, 1997; Walker et al., 1981; Wilson, 1985; Schumacher and Schmincke, 1990). Such deposits may also undergo syn- or post-emplacement densification and/or sintering (e.g. Michol et al., 2008). Fig. 1C shows the spectacular example of the Taupō Ignimbrite (New Zealand). Reworking of volcaniclastic deposits may also yield stratified structures, for example by lahars (e.g. Pierson et al., 1990; Douillet et al., 2013) or through aeolian remobilisation (e.g. Iriondo and Kröhlung, 2007).

On a larger scale, the sequential superposition of lavas (e.g. Applegarth et al., 2010), often interbedded with fall deposits, is ultimately responsible for constructing massive portions of a volcanic edifice. Indeed, the very definition of a stratovolcano implies anisotropy, in that a typical edifice is built up layers of volcanic material emplaced with a bedding orientation. Fig. 1D shows an example

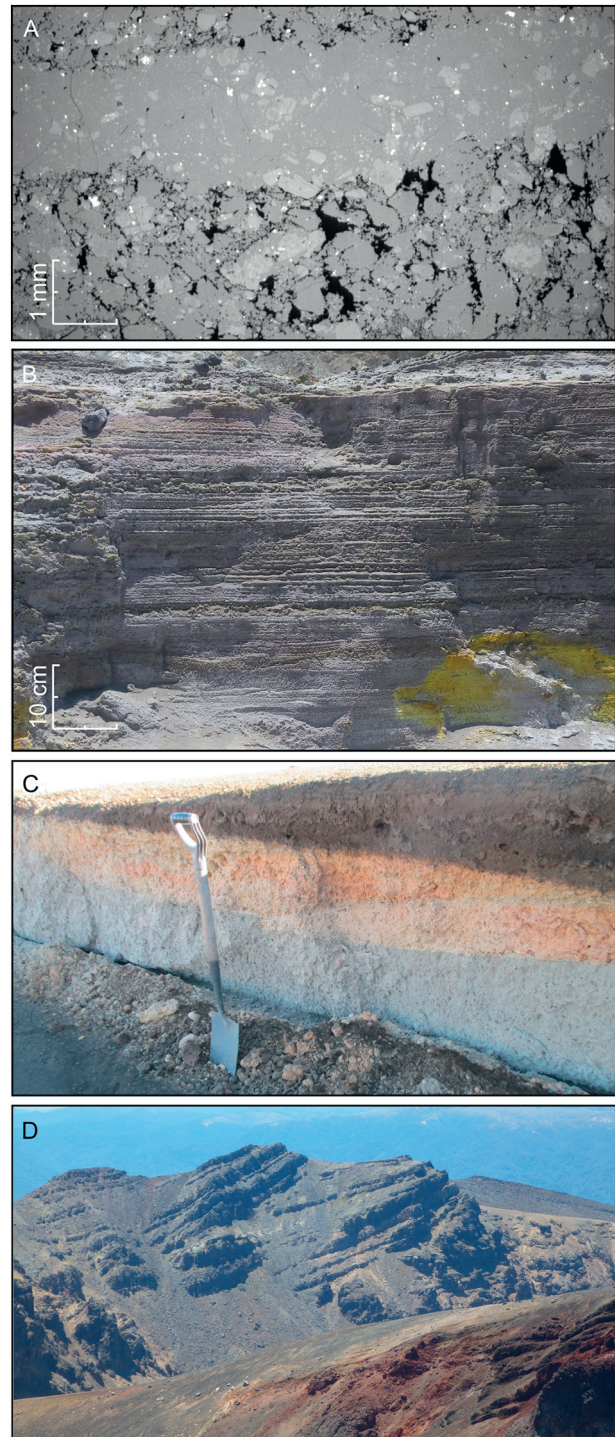


Fig. 1. Layering in volcanic environments over different scales. [A] Microstructural anisotropy in banded andesite from Volcán de Colima, Mexico (Farquharson et al., 2016). Scalebar is approximate, due to the “fisheye” effect at this magnification. [B] Finely bedded ash at Whakaari (White Island), New Zealand. Scale is approximate. [C] Layers of the Taupō Ignimbrite, New Zealand. Photo credit: Mike Heap. Spade for scale. [D] Tongariro Trig andesite lavas, photographed looking north from Red Crater towards Te Maari, Tongariro National Park, New Zealand.

of exposed strata, resulting from emplacement of massive lavas in the Tongariro Volcanic Centre (New Zealand).

Laboratory measurements of permeability on volcanic media often reflect this anisotropy, with the obtained value of permeability

depending on the orientation of the sample with respect to sample-scale heterogeneities. Heap et al. (2017a) show measurements of ash tuffs containing gas elutriation pipes, and note that permeability was generally (though not always) higher when fluid flow was parallel to the pipe orientation. Kendrick et al. (2014) found that the permeability of pseudotachylite-bearing andesite from Soufrière Hills volcano was approximately three orders of magnitude lower when the sample was prepared perpendicular to the pseudotachylite vein relative to a sample cored parallel to the vein. Similar magnitudes were reported by Okumura et al. (2009) who measured experimentally deformed rhyolitic melts perpendicular and parallel to shear induced through torsional deformation. Gaunt et al. (2014) measured permeability of samples from the marginal shear zone of the 2004–2008 lava dome at Mount St. Helens (USA), reporting permeability anisotropy of up to almost four orders of magnitude for sheared dacite and fault gouge. Wright et al. (2006, 2009) measured the permeability of suites of tube pumice–pumice containing a porous network of highly elongate bubbles with a preferred orientation—and noted the permeability was up to around two orders of magnitude higher when measured parallel to bubble elongation relative to samples prepared perpendicular to this. Additionally, Wright et al. (2009), by preparing and measuring samples at intermediate angles with respect to the bubble orientation, show that permeability of tube pumice is sensitive to the angle of anisotropy relative to the direction of imposed fluid flow.

Permeability of an anisotropic medium is often termed “equivalent” permeability, here $\langle k \rangle$, so-called because an anisotropic medium will have a permeability that is *hydraulically equivalent* to a conceptual homogeneous system (Freeze and Cherry, 1979; Renard and De Marsily, 1997). In this contribution, we outline the derivation of this property, and demonstrate—through theory and experiment—that the value of permeability differs with respect to the orientation relative to layering. Finally, we outline the importance of these observations in the context of modelling volcanic systems.

2. Theoretical background: permeability

Darcy's law (Darcy, 1856) is the constitutive equation governing fluid transport in porous or granular media in the low-Reynolds number regime. Originally derived from experiments performed by Henry Darcy in the 1850s, the theoretical framework of fluid transport—which is based on Newton's second law—has been well established and expanded in the years since.

At a constant elevation, Darcy's law is a proportional relationship between the steady-state discharge rate Q of a fluid of viscosity μ through a porous medium with cross-sectional area A . Flow is driven over a length L towards the low pressure region down a local pressure gradient ∇p . In the laboratory, the pressure gradient driving flow can be approximated as linear over the length L , and so this is defined as the pressure difference between a point of relatively high pressure p_b towards a point of relatively low pressure p_a . The value of this pressure gradient $p_b - p_a$ is given as Δp . In this case, Darcy's law is

$$Q = -\frac{kA}{\mu} \frac{p_b - p_a}{L} \quad \text{or} \quad Q = -\frac{kA}{\mu} \frac{\Delta p}{L} \quad (1)$$

where Q is in units of $\text{m}^3 \text{s}^{-1}$. We can divide both sides of the equation by the area A , giving a more general notation:

$$\mathbf{q} = -\frac{\mathbf{k}}{\mu} \nabla \mathbf{p} \quad (2)$$

where \mathbf{q} is the discharge per unit area—also referred to as flux or Darcy velocity—in units of m s^{-1} (the velocity of fluid flow \mathbf{v} through the porosity ϕ of the medium is related to the flux by $\mathbf{v} = \mathbf{q}/\phi$.)

The term $\nabla \mathbf{p}$ is the pressure gradient, equivalent to $\Delta p/L$ for small L and thus has units of Pa m^{-1} . For the sake of clarity, we drop formal vector notation throughout the remainder of this contribution.

2.1. Flow in three dimensions

In three dimensions, the initial Darcy velocity is resolved in three orthogonal directions in a Cartesian coordinate system x , y , and z , giving q_x , q_y , and q_z . Fundamentally, each of these components may exhibit a rate of change, which will depend on the direction in which the change is occurring. The difference between the velocity at any two given points is described by nine components which correspond to each of the directions x , y , and z . Thus

$$q_x = -\frac{k_{xx}}{\mu} \nabla p_{xx} - \frac{k_{xy}}{\mu} \nabla p_{xy} - \frac{k_{xz}}{\mu} \nabla p_{xz} \quad (3a)$$

$$q_y = -\frac{k_{yx}}{\mu} \nabla p_{yx} - \frac{k_{yy}}{\mu} \nabla p_{yy} - \frac{k_{yz}}{\mu} \nabla p_{yz} \quad (3b)$$

$$q_z = -\frac{k_{zx}}{\mu} \nabla p_{zx} - \frac{k_{zy}}{\mu} \nabla p_{zy} - \frac{k_{zz}}{\mu} \nabla p_{zz} \quad (3c)$$

2.2. Introducing anisotropy

Eqs. (3a)–(3c) highlight that permeability—in the most general case—similarly comprises nine components. Permeability at any given point may be expressed by $k = k(\theta)$, where θ is the angle between the horizontal plane and the direction of a measurement of permeability. There exists a mutually orthogonal set of directions where the angle θ corresponds to the maximum and minimum values of k : these are termed the “principal directions of anisotropy” (e.g. Renard et al., 2001).

If we array these components in a matrix, permeability becomes a symmetric second-rank tensor, known as the permeability tensor (Neuman, 1977):

$$\langle k \rangle = \begin{bmatrix} k_{xx} & k_{xy} & k_{xz} \\ k_{yx} & k_{yy} & k_{yz} \\ k_{zx} & k_{zy} & k_{zz} \end{bmatrix} \quad (4)$$

where each k_{ij} component corresponds to the coordinates in a Cartesian system. However, it is generally sufficient to assume that the xyz coordinate axes coincide with the principal directions of anisotropy. It follows that we lose the off-diagonal components: $k_{xy} = k_{xz} = k_{yx} = k_{yz} = k_{zx} = k_{zy} = 0$ (Neuman, 1977; Nabavati et al., 2009), giving us

$$\langle k \rangle = \begin{bmatrix} k_{xx} & 0 & 0 \\ 0 & k_{yy} & 0 \\ 0 & 0 & k_{zz} \end{bmatrix}. \quad (5)$$

Moreover, if we consider an anisotropic formation comprised of homogeneous layers—what we can refer to as a transversely isotropic layered medium—then we have $k_{xx} = k_{yy} \neq k_{zz}$. Fig. 2 illustrates such a conceptual layered medium.

In what follows we will present the analytical result for flow rate, and equivalent permeability, in the principal directions: (1) where the pressure gradient is acting parallel to the orientation of the layering, and (2) where the pressure gradient is acting perpendicular to the orientation of the layering. Then we will present a transformation for the permeability tensor that permits the calculation of the equivalent permeability in any orientation of interest.

Let us assume that each of the layers in the anisotropic system of dimensions $L \times L \times L$ (Fig. 2) is itself homogeneous in terms of its

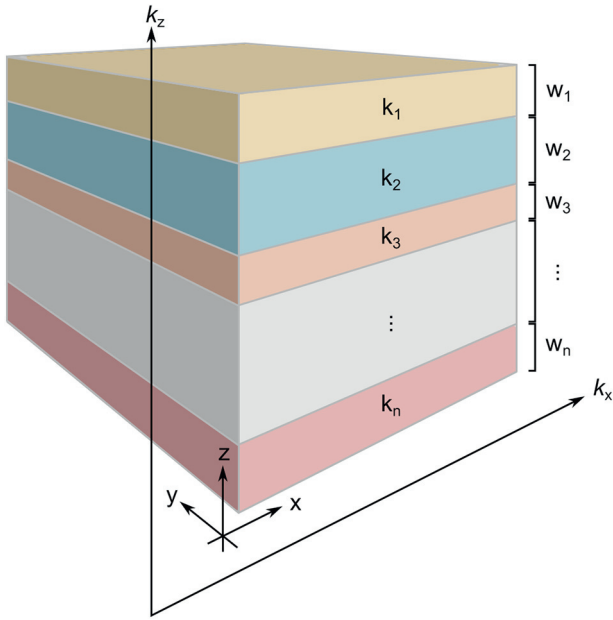


Fig. 2. A layered medium. Each of the layers constitutes a homogeneous unit with a width w_i and permeability k_i . Orientation of layers is such that they are parallel to x and y , and perpendicular to the z direction. $\langle k_x \rangle$ and $\langle k_z \rangle$ correspond to the permeability of the (entire) layered medium parallel and perpendicular to layering, respectively.

physical properties. Each layer has a given width $w_1, w_2, w_3, \dots, w_n$, where n is the total number of layers in the system. The total thickness of the system L may thus be given by the sum of all the layer widths:

$$L = \sum_{i=1}^n w_i \quad (6)$$

where w_i refers to the incremental layer width from $i = 1$ to n . Further, each layer has an isotropic permeability $k_1, k_2, k_3, \dots, k_n$.

3. Flow parallel to layering

When flow is parallel to the layering, each of the layers will have certain properties in common. Specifically, the length over which the pressure gradient occurs, the magnitude of the pressure gradient, and the fluid viscosity, will all be identical.

The bulk flow rate Q , however, will be partitioned over layers with widths $w_1, w_2, w_3, \dots, w_n$ such that their areas amount to the total cross-sectional area: $a_1 + a_2 + a_3 + \dots + a_n = A$. So, if i corresponds to a given layer, it is clear that $Q = \sum_{i=1}^n Q_i$ (where Q_i is the flow rate through layer i) and $A = \sum_{i=1}^n a_i$. Equivalently we can decompose the area into its constituent width w_i and length l components, giving: $A = \sum_{i=1}^n w_i l$. With these points in mind, we may now re-interrogate Darcy's law (Eq. (1)) leading us to

$$Q_1 = \frac{k_1 w_1 l \Delta p}{\mu L}, Q_2 = \frac{k_2 w_2 l \Delta p}{\mu L}, Q_3 = \frac{k_3 w_3 l \Delta p}{\mu L}, \dots, Q_n = \frac{k_n w_n l \Delta p}{\mu L}. \quad (7)$$

The equivalent permeability $\langle k_x \rangle$ corresponds to the total flow rate (the summation of flow rates through all individual layers), thus

$$Q \triangleq \sum_{i=1}^n Q_i = \frac{\langle k_x \rangle A \Delta p}{\mu L} = \left(\frac{k_1 w_1 l \Delta p}{\mu L} + \frac{k_2 w_2 l \Delta p}{\mu L} + \frac{k_3 w_3 l \Delta p}{\mu L} + \dots + \frac{k_n w_n l \Delta p}{\mu L} \right), \quad (8)$$

which simplifies and rearranges to

$$\langle k_x \rangle = \frac{\sum_{i=1}^n w_i k_i}{L}. \quad (9)$$

Eq. (9) is the “arithmetic mean” permeability, a weighted average dominated by the layers of highest permeability.

4. Flow perpendicular to layering

If we consider flow perpendicular to layering (i.e. flow in series, to draw an analogy with electrical circuits), then the volumetric flow rate Q must be equal entering and exiting the system. However, the overall pressure differential Δp is partitioned between layers of thickness $w_1, w_2, w_3, \dots, w_n$, becoming $\Delta p_1, \Delta p_2, \Delta p_3, \dots, \Delta p_n$. And so

$$\Delta p_1 = \frac{Q \mu w_1}{k_1 A}, \Delta p_2 = \frac{Q \mu w_2}{k_2 A}, \Delta p_3 = \frac{Q \mu w_3}{k_3 A}, \dots, \Delta p_n = \frac{Q \mu w_n}{k_n A} \quad (10)$$

In this case, the equivalent permeability $\langle k_z \rangle$ corresponds to the total pressure differential (the summation of pressure drops across all individual layers), thus

$$\Delta p \triangleq \sum_{i=1}^n \Delta p_i = \frac{Q \mu L}{\langle k_z \rangle A} = \left(\frac{Q \mu w_1}{k_1 A} + \frac{Q \mu w_2}{k_2 A} + \frac{Q \mu w_3}{k_3 A} + \dots + \frac{Q \mu w_n}{k_n A} \right) \quad (11)$$

which rearranges and simplifies to

$$\langle k_z \rangle = \frac{L}{\sum_{i=1}^n \frac{w_i}{k_i}} \quad \text{or} \quad \langle k_z \rangle = \frac{\sum_{i=1}^n w_i}{\sum_{i=1}^n \frac{w_i}{k_i}} \quad (12)$$

Eq. (12) is the “harmonic mean” permeability, a weighted average dominated by the layers of lowest permeability. As highlighted in Appendix A, it is assumed that all observations are positive real numbers: in practice, this means that the harmonic mean approach is valid as long as there are no wholly impermeable layers in the system.

5. Permeability in heterogeneous systems

Eqs. (9) and (12) correspond to the maximum and minimum equivalent permeabilities within a layered system, so it is to be expected that the equivalent permeability of any heterogeneous system will fall between these end-member values (e.g. Cardwell et al., 1945). For example, a commonly employed averaging method is the geometric mean:

$$\langle k_g \rangle = \left[\prod_{i=1}^n k_i^{w_i} \right]^{1/L} \quad (13)$$

which may be particularly useful for a case where the orientation is not strictly known.

Computational modelling (Warren and Price, 1961) has been used to show that $\langle k_g \rangle$ can provide a good representation of the equivalent permeability of a random heterogeneous medium. Nevertheless, care should be taken when applying the geometric mean equivalent permeability to highly heterogeneous systems (Jensen, 1991). A notable issue is that $\langle k_g \rangle \rightarrow 0$ when any of the constituent layers are close to impermeable, and unphysical values may be derived. Nevertheless, Jensen (1991)—based on theoretical approaches by Bakr et al. (1978), Gutjahr et al. (1978), Dagan (1979, 1981) amongst others—highlights that the geometric mean approach is a suitable means of assessing equivalent permeability if the measured permeabilities $k_1, k_2, k_3, \dots, k_n$ are log-normally distributed and display low variance. Jensen (1991) also introduces an approach termed the “*j*th Winsorized mean”, which involves removing so-called extreme values of k_i and replacing them with adjacently ranked data, prior to calculating $\langle k_g \rangle$.

For typical systems $\langle k_x \rangle > \langle k_g \rangle > \langle k_z \rangle$; indeed, for any given set of w_i and k_i , we can assert that $\langle k_x \rangle$ is greater than $\langle k_z \rangle$ (i.e. permeability parallel to layering in a natural system is *always* higher than permeability perpendicular to layering). A simple proof is offered in Appendix A, and we demonstrate this experimentally in the following section. Each of the averaging approaches discussed here are special cases of power-law averaging, a general analytical function. More complex power-law approaches have been employed to estimate hydraulic conductivity in previous studies, typically relating the conductivity of a system to the spatial correlation (or the degree thereof) of individual, variably permeable units. Such methods include spatial averaging (e.g. Deutsch, 1989) and renormalisation averaging (e.g. Piggott and Elsworth, 1992), but shall not be discussed further in this study.

In the context of upscaling permeability to applied systems, it is worth noting that these relatively simple averaging approaches may be further expanded in order to account for more complex system geometries. Both arithmetic and harmonic permeabilities may be applied to layered radial flow systems, for example, which could conceivably be of importance in volcanic and geothermal systems. In the first instance, fluid transport parallel to layering in a system of layered disks can be described by Eq. (9) without modification (Fig. 3A). Fluid transport perpendicular to layering in a system of annular units concentric to a central bore (representing a volcanic conduit or a geothermal well, for example) can be described by a modification of the harmonic average approach. In such a case, permeability must be weighted according to the distances of each concentric unit from the central point (e.g. Cardwell et al., 1945), therefore

$$\langle k_r \rangle = \ln\left(\frac{r_a}{r_b}\right) \sum_{i=1}^n \left[\ln\left(\frac{r_i}{r_{i-1}}\right) k_i^{-1} \right]^{-1}. \quad (14)$$

r_a and r_b are the central bore radius and the far-field radius, respectively. Values of r_i represent the incremental concentric radii of annular units. This is illustrated in Fig. 3B.

There are numerous scenarios wherein a volcanic edifice could be reasonably and usefully conceived as a transversely isotropic layered medium as illustrated in Fig. 3A. Stratovolcanoes are constructed from heterogeneous layers of eruptive material—which may possess distinct physical and mechanical properties (Gudmundsson and Brenner, 2004)—and are often modelled as such (e.g. Bakker et al., 2016). It has been observed that permeability may differ markedly depending on the subsurface stratigraphy (e.g. Watanabe et al., 2008). Indeed, even in a mechanically and compositionally homogeneous volcanic rock mass, permeability may be influenced by lithostatic pressure, effectively creating isobaric strata of differing

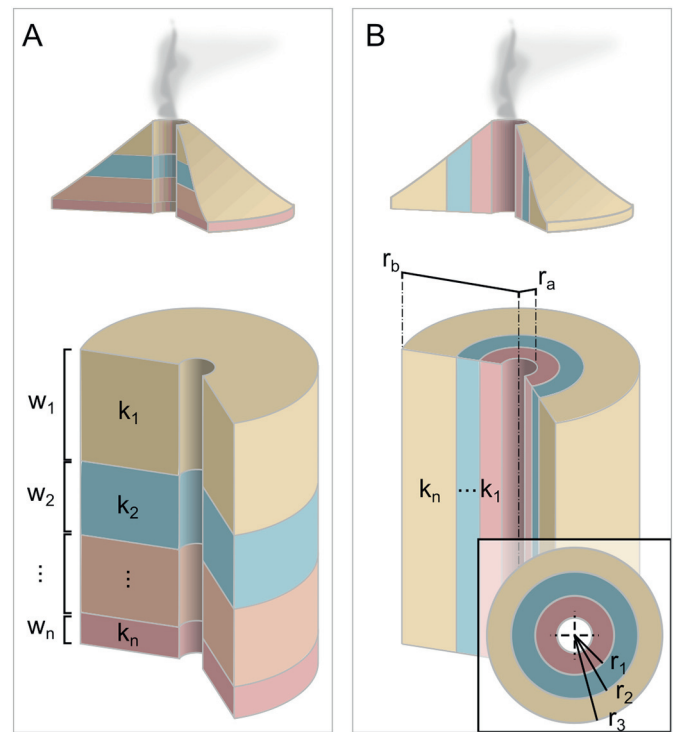


Fig. 3. Schematics of simple three-dimensional systems. [A] A system of layered disks, each with width w_1, w_2, \dots, w_n and corresponding values of permeability k_1, k_2, \dots, k_n . [B] A concentric annular system, where layers are described by their radii (e.g. r_1, r_2, r_3 : inset) with respect to the radii defining the system (r_a, r_b): those of the inner bore and the far-field radius, respectively. Cartoons highlight how these geometries could be applied to idealised volcanic systems. We emphasise that each cartoon represents a reductive simplification of a real volcanic system, with the schematics in the lower part of [A] and [B] representing the abstracted version of horizontally or vertically layered systems, respectively, presenting them in a more mathematically tractable form.

permeability. This is supported by experiments by Nara et al. (2011), amongst others.

Equally, there are circumstances where the permeability profile of a volcanic edifice may be imagined as an annular concentric structure (i.e. Fig. 3B). Shear in volcanic conduits is often posited to give rise to conduit-parallel strain localisation (e.g. Gonnermann and Manga, 2003; Tuffen and Dingwell, 2005; Plail et al., 2014). In turn, strain localisation in magma can influence permeability (e.g. Okumura et al., 2013; Farquharson et al., 2016). Further, volcano modelling (for example by Hurwitz et al., 2003; Lillis et al., 2015; Schauroth et al., 2016; Bakker et al., 2016; Heap et al., 2017b) often assumes a radial thermal gradient from the conduit into the edifice, a parameter which has been shown to influence permeability and permeability evolution (Gaunt et al., 2016; Kushnir et al., 2017b).

6. Calculating the equivalent permeability in layered systems at arbitrary angles relative to the fluid flow direction

In the above analysis, we have given the scaled solution for the equivalent permeability of a layered medium for the cases where the fluid flow is parallel to layering orientation, $\langle k_x \rangle$, and when the fluid flow is perpendicular to the layering orientation, $\langle k_z \rangle$. These represent the principal solutions, and allow us to write the permeability tensor as

$$\langle k \rangle = \begin{bmatrix} \langle k_x \rangle & 0 & 0 \\ 0 & \langle k_y \rangle & 0 \\ 0 & 0 & \langle k_z \rangle \end{bmatrix} \quad (15)$$

where we assume that both possible parallel directions are equal. The assumption of a transversely layered system (i.e. $k_x = k_y$) allows us to effectively reduce the permeability tensor to a 2D version as

$$\langle k \rangle = \begin{bmatrix} \langle k_x \rangle & 0 \\ 0 & \langle k_z \rangle \end{bmatrix}. \quad (16)$$

We can calculate the changes to the permeability tensor in Eq. (16) when the coordinate system is rotated by an angle θ . This effectively changes our xyz coordinate system to a new coordinate system, which we will term $\bar{x}\bar{y}\bar{z}$. To do this, we must define a transformation matrix for rotation of the Cartesian coordinates as follows:

$$\begin{bmatrix} x \\ z \end{bmatrix} = \begin{bmatrix} \cos(\theta) & \sin(\theta) \\ -\sin(\theta) & \cos(\theta) \end{bmatrix} \cdot \begin{bmatrix} \bar{x} \\ \bar{z} \end{bmatrix} \quad (17)$$

which, when applied to Eq. (16), yields a rotation of the tensor of the form

$$\langle k \rangle = \begin{bmatrix} k_a & k_b \\ k_c & k_d \end{bmatrix} \quad (18)$$

where $k_a = \langle k_x \rangle \sin^2(\theta) + \langle k_z \rangle \cos^2(\theta)$, $k_b = k_c = [\langle k_x \rangle - \langle k_z \rangle] \cos(\theta) \sin(\theta)$, and $k_d = \langle k_x \rangle \cos^2(\theta) + \langle k_z \rangle \sin^2(\theta)$. The choice of whether to use k_a or k_d depends on whether θ is measured from a horizontal or a vertical plane. Assuming the horizontal case, the result for fluid flow in a given direction, for which the layering is oriented at the angle θ from the x direction, gives the equivalent permeability of the system as k_d as follows:

$$\langle k \rangle = \langle k_z \rangle \sin^2(\theta) + \langle k_x \rangle \cos^2(\theta) \quad (19)$$

which has the desirable result that when $\theta = 0$, $\langle k \rangle = \langle k_x \rangle$, and when $\theta = \pi/2$, $\langle k \rangle = \langle k_z \rangle$. We note that it does not especially matter whether one uses k_a or k_d to define this, so long as the measurement of θ is adjusted accordingly. This result is of wide utility to volcanic scenarios in which the orientation of layering or fractures may be oblique to a principal flow direction for the permeating fluid, and provides a simple method to account for that situation. Moreover, it highlights that $\langle k_x \rangle$ and $\langle k_z \rangle$ require determination, presumably in the laboratory by measuring a suite of homogeneous rock samples that make up the constituent layers.

7. Anisotropy in natural volcanic samples

In the previous section we emphasise three separate but related points. First, we introduce the idea that permeability of a layered medium is always highest when measured parallel to its layering, and lowest when measured perpendicular. Second, we highlight that there are numerous weighted averaging methods which could feasibly be applied to permeability data measured on volcanic rocks at the laboratory scale in order to describe the system as a whole (i.e. on the edifice or conduit scale). We have focussed on three of these (the arithmetic, harmonic, and geometric means) with the idea that each most appropriately represents a different anisotropic configuration. Third, we provide a solution for the permeability at any arbitrary angle of the layering relative to the fluid flow direction by transforming the coordinate system, thus rotating the tensor and recomputing the permeabilities of each component.

The following subsections validate these concepts using measurements on natural volcanic materials. Note that the sample suites shown and discussed in the following sections exhibit significant differences in terms of their physical properties and the expression of

their sample-scale heterogeneities, a function of their differing origins. Rather than being comparative, these discrete case studies are illustrative of the points described above.

7.1. Soufrière Hills volcano banded pumice

We state that permeability parallel to layering must be greater than permeability perpendicular to layering. To demonstrate this, we provide measurements of permeability for a suite of variably banded pumice samples. The samples were cored from a single block, collected from the Belham River Valley on the island of Montserrat during a field campaign in 2012. The block is estimated to be derived from the 11 February 2010 partial collapse of the Soufrière Hills volcano dome, as described by Stinton et al. (2014). This block was selected because it demonstrates centimetric-scale banding, such that the derived samples exhibit relatively regular layering of lighter- and darker-coloured material (Fig. 4). Similarly heterogeneous pumice was noted following the 1997 explosive eruption of Soufrière Hills volcano by Burgisser et al. (2010) and others, as well as in other explosive volcanic environments around the globe (Venezky and Rutherford, 1997; Hall et al., 1999; Kennedy et al., 2005; Bouvet de la Maisonneuve et al., 2009; Farquharson et al., 2016). Whilst we presume the bands originated in the block of this study due to inhomogeneous bubble expansion or compaction whilst still deforming viscously prior to emplacement (e.g. Farquharson et al., 2016)—as a result of the complex decompression mechanisms associated with the 2011 dome collapse—we note that banding in pumice has been variously attributed to magma mingling (Venezky and Rutherford, 1997; Bouvet de la Maisonneuve et al., 2009), variations in magma differentiation (Hall et al., 1999), or variability in dissolved water content (Burgisser et al., 2010) as well as inhomogeneous bubble extension processes. Ultimately however, sleuthing out the physical mechanisms that generated the observed banding is not necessary for the analysis that follows. We highlight that we consider each sample as a medium composed of discrete layers, with each layer corresponding to a separate band.

Samples were prepared such that they had diameters of 20 mm and were nominally 40 mm in length (samples are shown in Fig. 4). Connected gas porosity ϕ was determined using helium pycnometry, and permeability was measured using a steady-state benchtop permeameter (see Heap and Kennedy, 2016; Farquharson et al., 2016, for a schematic). Uncertainty on the determination of porosity arises from (a) the precision of repeat automated pycnometry measurements and (b) error due to manual measurement of sample dimensions. Repeat measurements allow an estimation of error in the length and diameter, which typically amount to $<0.05 \text{ cm}^3$ in terms of volume. This corresponds to an average uncertainty on the porosity data of ± 0.004 , with a maximum of ± 0.009 (see Farquharson et al., 2017a, for details). Uncertainty on the determination of permeability is estimated to be $\pm 1\%$, and thus always falls within the symbol size when plotted graphically. Full details are provided in Appendix B. Table 1 displays the porosity and permeability data of the 20 samples.

Permeability is plotted against connected gas porosity for the Soufrière Hills volcano samples in Fig. 5. Clearly, the samples exhibiting layering parallel and perpendicular to the sample axis (and thus the direction of measurement: $\langle k_x \rangle$ and $\langle k_z \rangle$, respectively) comprise two distinct families on the graph, with the former tending to exhibit relatively higher permeability. The degree of scatter in these data is presumably a function of the naturally variable volume and geometry of the bands within the sample suite (as evident in Fig. 4). Nevertheless, these data highlight that permeability may vary significantly when anisotropy is investigated. For example, samples SHV-X-8 and SHV-Z-3, which have the same connected porosity (0.34) but were obtained and measured in orthogonal directions, differ by a factor of 5 in terms of their permeability (Table 1, Fig. 5).

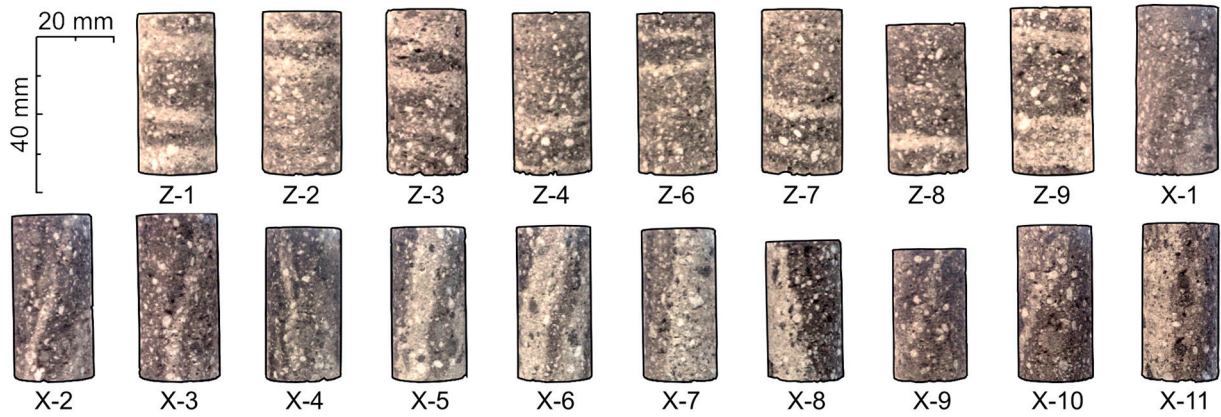


Fig. 4. Soufrière Hills volcano pumice samples. Note the alternating bands of lighter and darker colour evident in the samples (discussed further in the text). In this sample suite, the bands are variably anastomosing and sometimes diffuse, making accurate determination of their geometry non-trivial. Samples Z-1–Z-9 exhibit banding perpendicular to the sample axis. Samples X-1–X-11 exhibit banding parallel to the sample axis. Sample Z-5 could not be photographed.

7.2. Volcán de Colima flow-banded lava

Three permeability weighted averaging methods have been advanced in the preceding sections: arithmetic, harmonic, and geometric means (Eqs. (9), (12), and (13), respectively), with the assertion that they should best describe certain layered systems. To verify this, we use permeability data from cores of a flow-banded lava block collected from “El Volcancito”, a parasitic dome on the north-eastern flank of Volcán de Colima, Mexico (see Farquharson et al., 2016, for more information). The initial block was a dense lava exhibiting meso-scale anisotropy whereby half of the block appeared dark grey in colour and the other half was visibly lighter in colour (see Fig. 6; inset). Farquharson et al. (2016) prepared samples cored parallel and perpendicular to the interface between the two textures, including samples encompassing the interface in either orientation (Fig. 6).

Sample preparation and measurement were performed as described in the preceding section and Appendix B; however, the Forchheimer correction was not necessary for these data.

Due to the relatively simple geometry of the sample-scale heterogeneities, this sample suite can be used to assess the validity of the three permeability averaging approaches. For the layered samples

in either orientation, it should be possible to calculate their equivalent permeability $\langle k \rangle$ given knowledge of the width (or area, as appropriate) of either layer and their respective permeabilities.

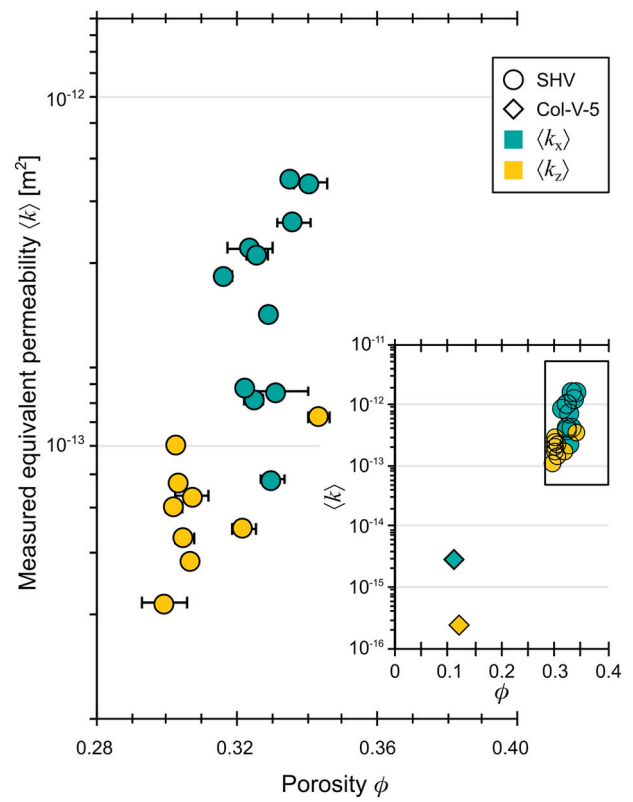


Fig. 5. Connected porosity and equivalent permeability data for volcanic samples cored parallel (green symbols) and perpendicular (yellow symbols) to sample-scale heterogeneities. Circles indicate Soufrière Hills volcano (SHV) banded pumice samples (see Table 1, Fig. 4). Note that the samples cored parallel to banding tend to exhibit higher permeabilities than those cored perpendicular, by up to around half an order of magnitude for the same porosity. Inset shows the Soufrière Hills volcano alongside samples of andesite exhibiting sample-scale anisotropy, collected from Volcán de Colima (Mexico). These data are discussed in more detail in the following section. Error calculation for porosity data is described in Farquharson et al. (2017a); for these data the average uncertainty is ± 0.004 , with a maximum of ± 0.009 . Maximum uncertainty on permeability data is $\pm 1\%$, which is smaller than the symbol size. Details on the calculation of uncertainty for permeability data are given in Appendix B.

Table 1

Connected porosity ϕ and permeability k data for 20 Soufrière Hills volcano banded pumice samples. Permeability was measured parallel \parallel or perpendicular \perp to banding.

Sample	ϕ	k [m^2]	Orientation
SHV-X-1	0.32	1.10×10^{-12}	\parallel
SHV-X-2	0.33	2.41×10^{-13}	\parallel
SHV-X-3	0.33	1.06×10^{-12}	\parallel
SHV-X-4	0.32	9.15×10^{-13}	\parallel
SHV-X-5	0.32	4.07×10^{-13}	\parallel
SHV-X-6	0.32	4.43×10^{-13}	\parallel
SHV-X-7	0.33	7.18×10^{-13}	\parallel
SHV-X-8	0.34	1.73×10^{-12}	\parallel
SHV-X-9	0.34	1.69×10^{-12}	\parallel
SHV-X-10	0.34	1.31×10^{-12}	\parallel
SHV-X-11	0.33	4.30×10^{-13}	\parallel
SHV-Z-1	0.30	1.07×10^{-13}	\perp
SHV-Z-2	0.32	1.74×10^{-13}	\perp
SHV-Z-3	0.34	3.63×10^{-13}	\perp
SHV-Z-4	0.30	2.01×10^{-13}	\perp
SHV-Z-5	0.31	1.64×10^{-13}	\perp
SHV-Z-6	0.30	2.35×10^{-13}	\perp
SHV-Z-7	0.31	1.41×10^{-13}	\perp
SHV-Z-8	0.30	3.02×10^{-13}	\perp
SHV-Z-9	0.31	2.16×10^{-13}	\perp

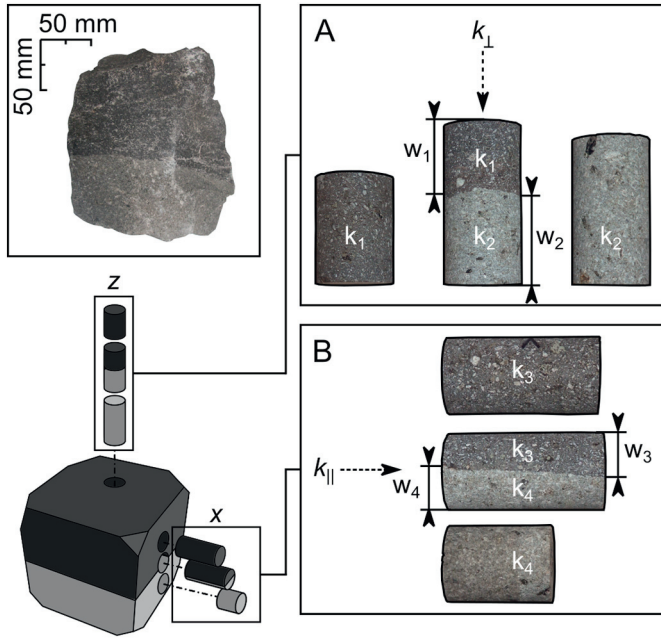


Fig. 6. Samples of Col-V-5 in z and x directions. [A] Three samples were cored in the z direction in the manner shown. [B] Three samples were cored in the x direction, as indicated in the sketch. The initial block is shown in inset. Permeability measured in the direction of the dashed arrow in either case. See Farquharson et al. (2016) for more information.

Fig. 6 shows the six samples discussed in this section. For the samples cored in the z direction (**Fig. 6A**), the permeabilities of the dark- and light-grey parts of the block are referred to as k_1 and k_2 , respectively. The permeability of the layered sample shall be given as $\langle k_{\perp} \rangle$: a function of the ratio of thickness of either component (w_1 and w_2), which were measured with digital callipers (**Table 2**). Similarly, for the samples cored in the x direction (**Fig. 6B**), the permeabilities of the dark- and light-grey parts of the block are referred to as k_3 and k_4 , respectively, and the equivalent permeability of the sample shall be referred to as k_{\parallel} . Due to the cylindrical geometry of the samples, we cannot simply use the w_3 and w_4 dimensions (**Fig. 6B**). Instead, we use the average cross-sectional area of each component (dark grey vs. light grey), which we present in **Table 2** as a_3 and a_4 . These values were determined by binarising digital photographs of either face of the sample, then normalising the output pixel area to the true total area of the cylindrical cross-section. We calculate w_3 and w_4 on either side of the sample (note that they differ: **Fig. 6**), and use

Table 2

Values used for calculating arithmetic, geometric, and harmonic mean permeabilities. $k_1 \dots k_4$ are permeabilities as indicated in **Fig. 6**. Along with the values of k_{\perp} and k_{\parallel} , these have been taken from Farquharson et al. (2016). w_1 and w_2 represent band thickness as shown in **Fig. 6**. a_3 and a_4 are cross-sectional areas of the bands represented by w_3 and w_4 , respectively, in **Fig. 6**. Refer to text for discussion.

Parameter	Value	Units
k_1	1.37×10^{-14}	m^2
k_2	2.90×10^{-16}	m^2
k_3	1.05×10^{-14}	m^2
k_4	6.24×10^{-16}	m^2
w_1	19.93 ± 3.75	mm
w_2	20.98 ± 3.75	mm
a_3	96.30 ± 24.13	mm^2
a_4	218.01 ± 24.13	mm^2
k_{\perp}	2.48×10^{-16}	m^2
k_{\parallel}	3.03×10^{-15}	m^2

the mean with an upper and lower bound (**Table 2**) for our subsequent calculations, with the standard deviation on that mean being a component of the uncertainty. For calculations, each w_i parameter in Eqs. (9), (12), and (13) was substituted for a_i , thereby translating the averages into two dimensions rather than one (e.g. Heap and Kennedy, 2016). All of the permeability data shown in **Table 2** are taken from Farquharson et al. (2016).

First, we shall look at the layered sample cored perpendicular to layering, k_{\perp} (see **Fig. 6A**). Accounting for potential inaccuracies in layer (band) geometry, the values determined using Eqs. (9), (12), and (13) are: $\langle k_x \rangle = 6.82 \times 10^{-15} \pm 1.23 \times 10^{-15} m^2$, $\langle k_z \rangle = 5.54 \times 10^{-16} \pm 8.11 \times 10^{-17} m^2$, and $\langle k_g \rangle = 1.90 \times 10^{-15} \pm 5.64 \times 10^{-16} m^2$, respectively. The true (measured) value is $k_{\perp} = 2.48 \times 10^{-16} m^2$.

For the sample cored parallel to layering, k_{\parallel} (see **Fig. 6B**), we obtain the following values for each of the averaging approaches (Eqs. (9), (12), and (13)): $\langle k_x \rangle = 3.65 \times 10^{-15} \pm 7.58 \times 10^{-17} m^2$, $\langle k_z \rangle = 8.77 \times 10^{-16} \pm 8.07 \times 10^{-17} m^2$, and $\langle k_g \rangle = 1.48 \times 10^{-15} \pm 2.89 \times 10^{-16} m^2$, respectively. The true (measured) value is: $k_{\parallel} = 3.03 \times 10^{-15} m^2$.

These data are shown graphically in **Fig. 7**. In both cases, $\langle k_x \rangle > \langle k_g \rangle > \langle k_z \rangle$, and there is no overlap between calculated values. For the perpendicular sample, k_{\perp} is lower than any of the calculated values; however, the harmonic mean $\langle k_z \rangle$ provides the closest estimate, as predicted. The discrepancy between the measured and calculated value here is perhaps due to variations in band thickness *inside* the sample, thus not reflected in the measured values of w_1 and w_2 . For the parallel sample, k_{\parallel} is exactly within the range calculated from the arithmetic mean, which—again—is consistent with our predicted result. Notably, using an inappropriate averaging method could yield results almost an order of magnitude away from the true value. Moreover, it is clear that should the geometric averaging method be employed in this instance, one might incorrectly assume that $k_{\perp} > k_{\parallel}$, which is evidently not the case. Nevertheless, if the precise geometry and orientation of an anisotropic medium is unknown, the geometric average may provide a reasonable compromise between the direction-specific arithmetic and harmonic averages (provided the caveats mentioned previously are adhered to: normal distribution and low variance of permeability).

7.3. Equivalent permeability at angles oblique to layering

We have used two end-members as a case study (banding is layered at $\pi/2$ and π (or 0) radians relative to the direction of fluid flow). If the orientation of anisotropy occurs at angles between $\pi/2$ and π rad (i.e. neither perpendicular nor parallel to the direction of fluid flow), the fluid flow properties become more complex. In such a case, the principal directions of anisotropy no longer coincide with the Cartesian xyz coordinate system, and we must use Eq. (19). The relative importance of the highest and lowest permeability layers is a function of the angle of anisotropy. Thus, steep-angle layering (orientation close to π) will exhibit $\langle k \rangle$ close to $\langle k_{\parallel} \rangle$ and shallow-angle layering (orientation close to $\pi/2$) will $\langle k \rangle$ close to $\langle k_{\perp} \rangle$. We give the solution to Eq. (19) on **Fig. 7A** as the dashed line.

As another test of this result, we present data from Wright et al. (2009) in **Fig. 7B**. Wright et al. (2009) measured a suite of samples cored from a single clast of anisotropic pumice from the Tumalo volcanic centre (USA). Their samples were prepared such that they were oriented at a range of orientations relative to bubble elongation. Their value of $\langle k_z \rangle = 3.4 \times 10^{-13} m^2$ is the value perpendicular to the orientation of the tube vesicles, whilst their value of $\langle k_x \rangle = 2.9 - 3.0 \times 10^{-11} m^2$ is the value parallel to the orientation of the tube vesicles. With these inputs to Eq. (19), we can then compare every data point collected for samples at intermediate angles relative to the orientation of the tube vesicles. We find reasonable agreement

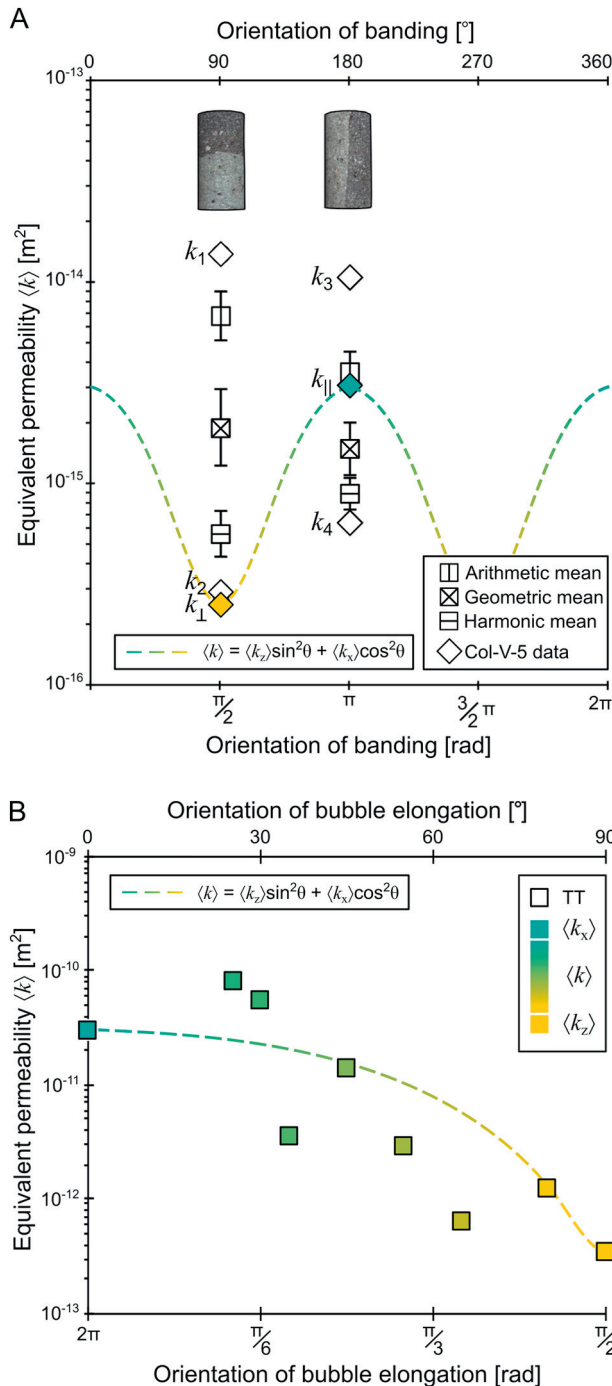


Fig. 7. [A] Measured and calculated permeability for banded lava, plotted versus the orientation of banding with respect to the sample axis. k_{\perp} and k_{\parallel} are given by the filled symbols, and the empty symbols indicate the values of k_i (Table 2). The range of values of the arithmetic, harmonic, and geometric means (based on the data in Table 2) are shown by the error bars (note that the average measurement error for the experimental data smaller than the size of the respective symbols: see Appendix B). Eq. (19) is plotted using the measured values of $\langle k_x \rangle$ and $\langle k_z \rangle$. Refer to text for discussion. [B] Data from Wright et al. (2009) for Tumalo tuff tube pumice (TT). Measurements were made at a range of angles with respect to bubble elongation. Dashed line shows Eq. (19), calculated using the data at $2\pi (\langle k_x \rangle)$ and $\pi/2$ rad ($\langle k_z \rangle$) from Wright et al. (2009).

with the function $\langle k \rangle = \langle k_x \rangle \sin^2(\theta) + \langle k_z \rangle \cos^2(\theta)$ (Eq. (19)). We note, however, that oriented bubbles are not strictly the same geometry as oriented layers discussed above. Nevertheless, these data serve as a useful demonstration.

8. An application to volcanic rock with fracture networks

We have established and explored a range of possible tools to scale from laboratory measurements on relatively homogeneous materials, to larger systems that are composed of layers that cannot usually be measured by laboratory methods, and which impart an anisotropy of permeability to the whole system. Here we discuss a possible extension to this scaling that we have not validated explicitly, but which would be of interest for volcanic settings.

Fractures are pervasive in volcanic environments—from the micro-scale to large fault structures and fissures (Varley and Taran, 2003; Tuffen and Dingwell, 2005; Gaunt et al., 2014)—and these probably exert a dominant influence over the overall permeability of a fracture-bearing volcanic rock (or magma) matrix. If we consider fractures as planar features, then they can be thought of as a layer like any other, with a constituent thickness, or width, w_f and permeability, k_f . Standard results for Poiseuille flow in a fracture-geometry can be rearranged with Darcy's law to give the permeability of an individual fracture (see Zimmerman and Bodvarsson, 1996):

$$k_f = H \frac{w_f^2}{12} \quad (20)$$

where H is an empirical roughness factor, which is $H = 1$ for smooth fractures (modified after Heap and Kennedy, 2016). This result can be used as one of the constituent layer permeabilities in the analysis presented above to determine the average permeability of the system. Treating a fractured mass as a two-component system (i.e. a matrix of permeability k_m and a series of fractures with total width $\sum_{i=1}^n w_{f_i}$), Eqs. (9) and (12) become

$$\langle k_x \rangle = \left[k_m \underbrace{\left(L - \sum_{i=1}^n w_{f_i} \right)}_{\text{matrix}} + \sum_{i=1}^n w_{f_i} \underbrace{\sum_{i=1}^n \frac{w_{f_i}^2}{12}}_{\text{fractures}} \right] \times \left[\frac{1}{L} \right] \quad (21)$$

and

$$\langle k_z \rangle = L \times \left[\underbrace{\left(\frac{L - \sum_{i=1}^n w_{f_i}}{k_m} \right)}_{\text{matrix}} + \underbrace{\left(\sum_{i=1}^n \frac{w_{f_i}^{-1}}{12} \right)}_{\text{fractures}} \right]^{-1} \quad (22)$$

where the components that refer to the matrix and fractures are labelled. As with the previous examples, permeabilities at arbitrary intermediate angles can then be calculated using Eq. (19). This is illustrated in Fig. 8. Note that Eqs. (21) and (22) show

$$\langle k \rangle \rightarrow \sum_{i=1}^n \frac{w_{f_i}^2}{12} \quad \text{as} \quad \left(L - \sum_{i=1}^n w_{f_i} \right) \rightarrow 0 \quad (23)$$

and

$$\langle k \rangle \rightarrow k_m \quad \text{as} \quad \sum_{i=1}^n w_{f_i} \rightarrow 0. \quad (24)$$

More generally, $\langle k \rangle \rightarrow k_i$ as $(L - w_i) \rightarrow 0$.

Fig. 8A shows an outcrop at the dacitic Ceboruco lava dome (Nayarit, Mexico). Highlighted is a 1×1 m area of dense lava containing several nominally planar fractures oriented at an oblique angle to vertical (with respect to the photograph and its current orientation). We use this outcrop to demonstrate the importance of

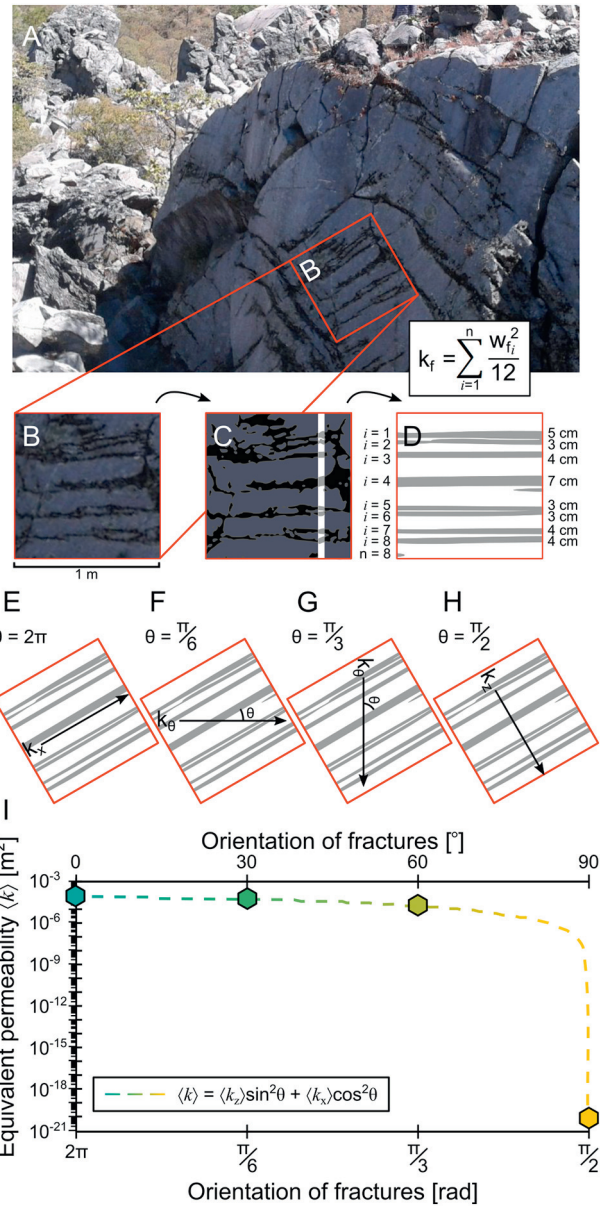


Fig. 8. Arithmetic and harmonic mean permeabilities of a fractured medium can be determined if the number n and width w_f of fractures within a homogeneous matrix are known. [A] Photograph of part of the Ceboruco lava dome (Mexico). Highlighted box is 1×1 m. [B] Close-up of the selected area, which is then binarised [C] and simplified [D] for the purposes of this analysis. [E]–[H] illustrate the different values of θ when considering equivalent permeability in different orientations. [E] Equivalent permeability parallel to the fracture orientation is $\langle k_x \rangle$ of the medium, and can be calculated from Eq. (21). [F] Permeability along the horizontal plane. [G] Permeability along the vertical plane. [H] Equivalent permeability perpendicular to the fracture orientation is $\langle k_z \rangle$ of the medium, and can be calculated from Eq. (22). Once $\langle k_x \rangle$ and $\langle k_z \rangle$ have been calculated, intermediate angles [F]–[G] can be determined using Eq. (19). [I] shows the modelled results for $\langle k \rangle$ vs fracture angle.

fractures in governing the permeability of a large rock mass. The fractured area is shown in more detail in Fig. 8B, which we binarise (Fig. 8C) and further simplify (Fig. 8D) in order to estimate the fracture widths. Of $n = 8$ fractures, fracture widths range from 0.03 to 0.07 m. From Eq. (20), these widths reflect permeabilities ranging from 7.50×10^{-5} and $4.08 \times 10^{-4} \text{ m}^2$. If we assume that the host rock has a permeability of 10^{-21} m^2 , then we can calculate the values of $\langle k_x \rangle$ (Fig. 8E) and $\langle k_z \rangle$ (Fig. 8H) after Eqs. (21) and (22), respectively. Similarly, Eq. (19) can be employed to determine the

permeability at oblique angles $\theta = \pi/6 \text{ rad}$ (Fig. 8F) and $\theta = \pi/3 \text{ rad}$ (Fig. 8G). For this simple example, $\langle k_x \rangle = 6.18 \times 10^{-5} \text{ m}^2$, highlighting the important influence of fractures in controlling fracture-parallel fluid flow. Perpendicular to the fracture orientation, $\langle k_z \rangle = 1.49 \times 10^{-21} \text{ m}^2$: only marginally higher than the permeability of the matrix k_m . The equivalent permeability calculated in the horizontal ($\theta = \pi/6 \text{ rad}$) and vertical ($\theta = \pi/3 \text{ rad}$) directions are 4.63×10^{-5} and $1.54 \times 10^{-5} \text{ m}^2$, respectively. Critically, these are evidently much closer to $\langle k_x \rangle$ than $\langle k_z \rangle$: a fact that should be borne in mind when measuring laboratory-scale samples.

Certainly, this rudimentary example does not reflect a number of components of the natural system. The fracture aperture is rarely constant along the length of a fracture (i.e. $H \neq 1$), even in the vastly simplified example above. In a recent study, Heap and Kennedy (2016) calculated fracture permeabilities in samples of andesite to be on the order of 10^{-10} – 10^{-9} m^2 for their sample size (on the order of 0.02 m), which highlights that the idealised geometry assumed by Eq. (20) does not capture the complexities of variably tortuous, non-planar fractures. Note that if we were to scale the example above to reflect the sample size of Heap and Kennedy (2016) (i.e. with the same ratio w_f/L but over a smaller length scale), then a value of H around 0.01 would be sufficient to bring the fracture permeabilities calculated using Eq. (20) in line with their experimentally-derived range. Additionally, this analysis has only accounted for the surface expression of the fractures, whereas a more in-depth assessment of the permeability of the dome would require some assumption of the internal fracture architecture of the rock mass, and how this changes with depth (i.e. confining pressure). Nevertheless, this analysis emphasises the significant contribution of fractures to fluid flow in otherwise low-permeability volcanic material, something that is not necessarily reflected in laboratory-based studies. Given the proliferation of permeability data collected for volcanic materials in recent years, incorporating them into models that reflect the natural anisotropy extant in volcanic systems ought to become commonplace. We anticipate that the relatively simple formulations described throughout this study can prove to be useful tools to this end.

9. Concluding remarks

Using laboratory measurements on two suites of anisotropic volcanic rocks, we have demonstrated two fundamental points to account for when considering permeability in anisotropic volcanic systems.

1. First, whenever a layered medium contains layers with different permeabilities, the permeability parallel to layering will always be higher than that measured perpendicular.
2. Secondly, the choice of averaging method used to upscale permeability data is of great importance. Our data highlight that employing an inappropriate upscaling approach can result in data that are erroneous by almost an order of magnitude (for the samples tested in this study). Significantly, using an inappropriate averaging method can result in values that are contrary to point 1.

We have highlighted scenarios where a volcano could be modelled as a vertically or horizontally layered medium (in two dimensions) or layered disks or an annular concentric medium (in three dimensions), depending on the variables under consideration. As shown both by theory and our data, the averaging method used to estimate equivalent permeability—an imperative step for transferring permeability from the laboratory- to model-scale—can exert a significant influence on the ultimate values derived. As an additional step, we have accounted for any oblique angle of fluid flow relative to the layering in the large rock mass, and validated this against our

data and data for tube pumices compiled from Wright et al. (2009). Finally, we also provide solutions to calculate estimate equivalent permeability of a fractured rock mass at all angles relative to the planar fracture direction, assuming that the matrix permeability is known. In concert, these results provide tools to upscale from suites of measurements collected using individual rock samples, to larger systems composed of layers with or without fractures.

We urge that future models that include edifice and/or conduit permeability as a variable account for the potential for significant permeability anisotropy in these systems. Moreover, we recommend that the simple formulations described herein be used to transfer the wealth of laboratory data collected on volcanic media to scales that are relevant for edifice-scale modelling.

Acknowledgements

We thank Jackie Kendrick and Jérémie Vasseur for constructive reviews and Joan Martí for editorial handling. Mike Heap and Nick Varley are thanked for assistance in the field in Mexico, and Mike is additionally thanked for his assistance during sample preparation and characterisation. A large team, including Yan Lavallée, Betty Scheu, Paul Cole, Linda Petrokova, Jackie Kendrick and Jérémie Vasseur helped collect the samples from the island of Montserrat. This paper benefited from conversations with Luke Griffiths, Ed Llewellyn, Alex Kushnir, and Bec Fitzgerald.

Appendix A. Arithmetic mean is always greater than the harmonic mean in an anisotropic medium: proof

This appendix outlines a proof of the assertion that the arithmetic mean of a set of values (such as permeability measurements) is always greater than the harmonic mean of the same set. For a more comprehensive proof, please refer to Binmore (1982).

We may define the arithmetic mean $\langle x \rangle$ of a set of measurements or observations $x_1, x_2, x_3, \dots, x_n$ as

$$\langle x \rangle = \frac{1}{n} \left(\sum_{i=1}^n x_i \right) \quad (\text{A.1})$$

as long as the observations are positive real numbers (i.e. $x_1, x_2, x_3, \dots, x_n \in \mathbb{R}_{>0}$). The harmonic mean $\langle z \rangle$ may be cast as

$$\frac{1}{\langle z \rangle} = \frac{1}{n} \left(\sum_{i=1}^n \frac{1}{x_i} \right) \quad (\text{A.2})$$

for all values of i that are positive real numbers ($\forall i \in [1 \dots n] : x_i > 0$). Fundamentally, these expressions (Eqs. (A.1) and (A.2)) are the same as Eqs. (9) and (12). The corollary of the positive real numbers caveat is that both $\langle x \rangle$ and $\langle z \rangle$ may be expressed as a squared quantity:

$$\forall i \in [1 \dots n] : x_i = y_i^2. \quad (\text{A.3})$$

This gives us

$$\langle x \rangle = \frac{1}{n} \left(\sum_{i=1}^n y_i^2 \right) \quad \text{and} \quad \frac{1}{\langle z \rangle} = \frac{1}{n} \left(\sum_{i=1}^n \frac{1}{y_i^2} \right) \quad (\text{A.4})$$

If we multiply these two expressions together:

$$\langle x \rangle \times \frac{1}{\langle z \rangle} = \frac{\langle x \rangle}{\langle z \rangle} = \frac{1}{n^2} \left(\sum_{i=1}^n y_i \sum_{i=1}^n \frac{1}{y_i} \right)^2 \quad (\text{A.5})$$

Cauchy's inequality (in vector form: $\|\mathbf{a}\| \|\mathbf{b}\| \geq \|\mathbf{a} \cdot \mathbf{b}\|$) tells us that

$$\frac{1}{n^2} \left(\sum_{i=1}^n y_i \sum_{i=1}^n \frac{1}{y_i} \right)^2 \geq \frac{1}{n^2} \left(\sum_{i=1}^n \frac{y_i}{y_i} \right)^2 \quad (\text{A.6})$$

The right-hand-side reduces to unity, giving

$$\frac{\langle x \rangle}{\langle z \rangle} \geq 1 \quad (\text{A.7})$$

and finally

$$\langle x \rangle \geq \langle z \rangle. \quad (\text{A.8})$$

As the equality of $\langle x \rangle = \langle z \rangle$ (in the context of a permeable system $\langle k_x \rangle = \langle k_z \rangle$) requires a homogenous system, we can thus state that for any anisotropic system, $\langle k_x \rangle > \langle k_z \rangle$.

Appendix B. Determination of Darcian permeability at moderate Reynolds number or using compressible gas as the permeating fluid

When using a compressible gas as the permeant fluid, it becomes convenient to present permeability measured under near-atmospheric conditions in the form (Klinkenberg, 1941; McPhee and Arthur, 1991)

$$k_{\text{gas}} = \frac{Q \mu L \cdot p_{\text{atm}}}{A \cdot \Delta p \bar{p}}. \quad (\text{B.1})$$

Functionally the same as Eq. (1), the above form describes the driving force for flow in terms of a driving pressure $\Delta p \bar{p}$ and a downstream pressure (which in our case is atmospheric pressure p_{atm}) at which Q is measured. The mean pressure \bar{p} is a function of the upstream and downstream pressures p_b and p_a (as described in Farquharson et al., 2017a). We measured gas permeability using a modified steady-state benchtop permeameter as described in (Heap and Kennedy, 2016; Farquharson et al., 2016). Using nitrogen, a radial confining pressure of 1 MPa was applied to each sample; gas flow was induced through the sample after a suitable equilibration time using a pressure regulator connected to a cylinder of compressed gas. For different imposed pressure differentials Δp (measured using a pressure gauge connected inline upstream of the sample), the volumetric flow rate Q was measured with an El-Flow volumetric flowmeter and recorded with a purpose-built data acquisition system. With knowledge of the constants in Eq. (B.1) (i.e. sample dimensions, atmospheric pressure downstream of the sample, gas viscosity), k_{gas} could then be calculated, assuming laminar flow. On a graph of Q versus $\Delta p \bar{p}$ (the driving pressure), data should follow a linear trend (in the case of laminar flow); as such, the r^2 value of a straight line fit through $(Q, \Delta p \bar{p})$ pairs for each sample gives an assessment of the average measurement error (a function of finite transducer resolution and fluctuations in ambient conditions). We arbitrarily impose an threshold of $r^2 = 0.99$, meaning that calculations are only made from precise data. Ultimately this results in maximum uncertainties of $\pm 1\%$ for our permeability data (note that in most cases, $r^2 \gg 0.99$). This is typically much smaller than the symbol size when plotted graphically. However, in these high-porosity pumice samples, inertial forces were high (flow was turbulent). As a result, the “true” permeability is lower than the apparent (measured) permeability, as turbulence induces drag. As such, an auxiliary correction was

required. The so-called Forchheimer correction, after Forchheimer (1901) introduces an inertial term ι , such that

$$\frac{1}{k_{\text{Fo}}} = \frac{1}{k_{\text{gas}}} - \iota Q \quad (\text{B.2})$$

where k_{Fo} is the Forchheimer-corrected permeability value, and k_{gas} is the as-measured value (using gas). This correction is described more fully in Farquharson et al. (2017a). Note that in the case of turbulent flow, the graph of volumetric flow rate versus driving pressure would *not* be linear. However, a plot of the reciprocal of measured permeability k_{gas}^{-1} against Q will be linear in the absence of additional compounding factors. We impose the same r^2 threshold to these data, obtaining the same average measurement error.

References

- Applegarth, L., Pinkerton, H., James, M., Calvari, S., 2010. Lava flow superposition: the reactivation of flow units in compound 'a'ā flows. *J. Volcanol. Geotherm. Res.* 194, 100–106. <https://doi.org/10.1016/j.jvolgeores.2010.05.001>.
- Ashwell, P., Kendrick, J., Lavallée, Y., Kennedy, B., Hess, K.-U., Aulock, F., Wadsworth, F., Vasseur, J., Dingwell, D., 2015. Permeability of compacting porous lavas. *J. Geophys. Res. Solid Earth* 120, 1605–1622.
- Bagdassarov, N.S., Dingwell, D.B., 1992. A rheological investigation of vesicular rhyolite. *J. Volcanol. Geotherm. Res.* 50, 307–322.
- Bakker, R.R., Frehner, M., Lupi, M., 2016. How temperature-dependent elasticity alters host rock/magmatic reservoir models: a case study on the effects of ice-cap unloading on shallow volcanic systems. *Earth Planet. Sci. Lett.* 456, 16–25.
- Bakr, A.A., Gelhar, L.W., Gutjahr, A.L., MacMillan, J.R., 1978. Stochastic analysis of spatial variability in subsurface flows: 1. Comparison of one-and three-dimensional flows. *Water Resour. Res.* 14, 263–271.
- Binmore, K.G., 1982. Mathematical Analysis: A Straightforward Approach. Cambridge University Press.
- Bouvet de la Maisonneuve, C., Bachmann, O., Burgisser, A., 2009. Characterization of juvenile pyroclasts from the Kos Plateau Tuff (Aegean Arc): insights into the eruptive dynamics of a large rhyolitic eruption. *Bull. Volcanol.* 71, 643.
- Burgisser, A., Poussineau, S., Arbaret, L., Druitt, T.H., Giachetti, T., Bourdier, J.-L., 2010. Pre-explosive conduit conditions of the 1997 vulcanian explosions at Soufrière Hills Volcano, Montserrat: I. Pressure and vesicularity distributions. *J. Volcanol. Geotherm. Res.* 194, 27–41.
- Cardwell, W., Jr Parsons, R., et al. 1945. Average permeabilities of heterogeneous oil sands. *Trans. AIME* 160, 34–42.
- Caricchi, L., Burlini, L., Ulmer, P., Gerya, T., Vassalli, M., Papale, P., 2007. Non-Newtonian rheology of crystal-bearing magmas and implications for magma ascent dynamics. *Earth Planet. Sci. Lett.* 264, 402–419.
- Cashman, K.V., Thornber, C.R., Pallister, J.S., 2008. From dome to dust: shallow crystallization and fragmentation of conduit magma during the 2004–2006 dome extrusion of Mount St. Helens, Washington. *US Geol. Surv. Prof. Pap.* 387–413.
- Chevalier, L., Collombet, M., Pinel, V., 2017. Temporal evolution of magma flow and degassing conditions during dome growth, insights from 2D numerical modeling. *J. Volcanol. Geotherm. Res.* 333, 116–133.
- Chevrel, M., Platz, T., Hauber, E., Baratoux, D., Lavallée, Y., Dingwell, D., 2013. Lava flow rheology: a comparison of morphological and petrological methods. *Earth Planet. Sci. Lett.* 384, 109–120.
- Chevrel, M.O., Cimarelli, C., deBiasi, L., Hanson, J.B., Lavallée, Y., Arzilli, F., Dingwell, D.B., 2015. Viscosity measurements of crystallizing andesite from Tungurahua volcano (Ecuador). *Geochem. Geophys. Geosyst.* 16, 870–889.
- Christie, M., Blunt, M., et al. 2001. Tenth SPE comparative solution project: a comparison of upscaling techniques. SPE Reservoir Simulation Symposium. Society of Petroleum Engineers.
- Collinson, A., Neuberg, J., 2012. Gas storage, transport and pressure changes in an evolving permeable volcanic edifice. *J. Volcanol. Geotherm. Res.* 243, 1–13.
- Collombet, M., 2009. Two-dimensional gas loss for silicic magma flows: toward more realistic numerical models. *Geophys. J. Int.* 177, 309–318.
- Dagan, G., 1979. Models of groundwater flow in statistically homogeneous porous formations. *Water Resour. Res.* 15, 47–63.
- Dagan, G., 1981. Analysis of flow through heterogeneous random aquifers by the method of embedding matrix: 1. Steady flow. *Water Resour. Res.* 17, 107–121.
- Darcy, H., 1856. Les fontaines publiques de la ville de Dijon: Exposition et application des principes à suivre et des formules à employer dans les questions de distribution d'eau. [Exhibition and implementation of the principles to follow and the formulae to employ in the issue of water distribution]. Victor Dalmont, France. (In French).
- DeGruyter, W., Bachmann, O., Burgisser, A., 2010. Controls on magma permeability in the volcanic conduit during the climactic phase of the Kos Plateau Tuff eruption (Aegean Arc). *Bull. Volcanol.* 72, 63.
- Deutsch, C., 1989. DECLUS: a FORTRAN 77 program for determining optimum spatial declustering weights. *Comput. Geosci.* 15, 325–332.
- Douillet, G.A., Tsang-Hin-Sun, È., Kueppers, U., Letort, J., Pacheco, D.A., Goldstein, F., Aulock, F.V., Lavallée, Y., Hanson, J.B., Bustillos, J., Robin, C., Ramón, P., Hall, M., Dingwell, D.B., 2013. Sedimentology and geomorphology of the deposits from the August 2006 pyroclastic density currents at Tungurahua volcano, Ecuador. *Bull. Volcanol.* 75, <https://doi.org/10.1007/s00445-013-0765-7>.
- Eichelberger, J., Carrigan, C., Westrich, H., Price, R., 1986. Non-explosive silicic volcanism. *Nature* 323, 598–602.
- Farquharson, J.I., Baud, P., Heap, M.J., 2017a. Inelastic compaction and permeability evolution in volcanic rock. *Solid Earth* 8, 561.
- Farquharson, J.I., Heap, M.J., Lavallée, Y., Varley, N.R., Baud, P., 2016. Evidence for the development of permeability anisotropy in lava domes and volcanic conduits. *J. Volcanol. Geotherm. Res.* 323, 163–185.
- Farquharson, J.I., Heap, M.J., Varley, N.R., Baud, P., Reuschlé, T., 2015. Permeability and porosity relationships of edifice-forming andesites: a combined field and laboratory study. *J. Volcanol. Geotherm. Res.* 297, 52–68.
- Farquharson, J.I., Wadsworth, F.B., Heap, M.J., Baud, P., 2017b. Time-dependent permeability evolution in compacting volcanic fracture systems and implications for gas overpressure. *J. Volcanol. Geotherm. Res.* 339, 81–97.
- Forchheimer, P., 1901. Wasserbewegung durch boden [water movement through soil]. *Z. Ver. Dtsch. Ing.* 45, 1782–1788. (In German).
- Freeze, R.A., Cherry, J.A., 1979. Groundwater. 604 pp.
- Gaunt, H.E., Sammonds, P.R., Meredith, P.G., Chadderton, A., 2016. Effect of temperature on the permeability of lava dome rocks from the 2004–2008 eruption of Mount St. Helens. *Bull. Volcanol.* 78, 30.
- Gaunt, H.E., Sammonds, P.R., Meredith, P.G., Smith, R., Pallister, J.S., 2014. Pathways for degassing during the lava dome eruption of Mount St. Helens 2004–2008. *Geology* 42, 947–950. <https://doi.org/10.1130/g35940.1>.
- Gingras, M.K., Baniak, G., Gordon, J., Hovikoski, J., Konhauser, K.O., Croix, A.I., Lemiski, R., Mendoza, C., Pemberton, S.G., Polo, C., Zonneveld, J.-P., 2012. Porosity and permeability in bioturbated sediments. *Dev. Sedimentol.* Elsevier, pp. 837–868. <https://doi.org/10.1016/b978-0-444-53813-0.00027-7>.
- Giordano, D., Russell, J.K., Dingwell, D.B., 2008. Viscosity of magmatic liquids: a model. *Earth Planet. Sci. Lett.* 271, 123–134.
- Gonnermann, H., Manga, M., 2003. Explosive volcanism may not be an inevitable consequence of magma fragmentation. *Nature* 426, 432–435.
- Gudmundsson, A., Brenner, S.L., 2004. How mechanical layering affects local stresses, unrests, and eruptions of volcanoes. *Geophys. Res. Lett.* 31,
- Gutjahr, A.L., Gelhar, L.W., Bakr, A.A., MacMillan, J.R., 1978. Stochastic analysis of spatial variability in subsurface flows: 2. Evaluation and application. *Water Resour. Res.* 14, 953–959.
- Hall, M.L., Robin, C., Beate, B., Mothes, P., Monzier, M., 1999. Tungurahua volcano, Ecuador: structure, eruptive history and hazards. *J. Volcanol. Geotherm. Res.* 91, 1–21.
- Heap, M., Farquharson, J.I., Wadsworth, F., Kolzenburg, S., Russell, J., 2015. Timescales for permeability reduction and strength recovery in densifying magma. *Earth Planet. Sci. Lett.* 429, 223–233.
- Heap, M.J., Kennedy, B.M., 2016. Exploring the scale-dependent permeability of fractured andesite. *Earth Planet. Sci. Lett.* 447, 139–150.
- Heap, M.J., Kennedy, B.M., Farquharson, J.I., Ashworth, J., Mayer, K., Letham-Brake, M., Reuschlé, T., Gilg, H.A., Scheu, B., Lavallée, Y., et al. 2017a. A multidisciplinary approach to quantify the permeability of Whakaari/White Island volcanic hydrothermal system (Taupo Volcanic Zone, New Zealand). *J. Volcanol. Geotherm. Res.* 332, 88–108.
- Heap, M.J., Violay, M., Wadsworth, F.B., Vasseur, J., 2017b. From rock to magma and back again: the evolution of temperature and deformation mechanism in conduit margin zones. *Earth Planet. Sci. Lett.* 463, 92–100.
- Hurwitz, S., Kipp, K.L., Ingebritsen, S.E., Reid, M.E., 2003. Groundwater flow, heat transport, and water table position within volcanic edifices: implications for volcanic processes in the cascade range. *J. Geophys. Res. Solid Earth* 108,
- Iriondo, M., Kröhlung, D., 2007. Non-classical types of loess. *Sediment. Geol.* 202, 352–368. <https://doi.org/10.1016/j.sedgeo.2007.03.012>.
- Jaupart, C., 1998. Gas loss from magmas through conduit walls during eruption. *Geol. Soc. Lond. Spec. Publ.* 145, 73–90.
- Jensen, J., Glasbey, C., Corbett, P., 1994. On the interaction of geology, measurement, and statistical analysis of small-scale permeability measurements. *Terra Nova* 6, 397–403.
- Jensen, J.L., 1991. Use of the geometric average for effective permeability estimation. *Math. Geol.* 23, 833–840.
- Kendrick, J.E., Lavallée, Y., Hess, K.U., Angelis, S.D., Ferk, A., Gaunt, H.E., Meredith, P.G., Dingwell, D.B., Leonhardt, R., 2014. Seismogenic frictional melting in the magmatic column. *Solid Earth* 5, 199–208. <https://doi.org/10.5194/se-5-199-2014>.
- Kennedy, B., Spieler, O., Scheu, B., Kueppers, U., Taddeucci, J., Dingwell, D.B., 2005. Conduit implosion during vulcanian eruptions. *Geology* 33, 581–584.
- Klinkenberg, L., 1941. The permeability of porous media to liquids and gases. *Drilling and Production Practice*. American Petroleum Institute.
- Klug, C., Cashman, K.V., 1996. Permeability development in vesiculating magmas: implications for fragmentation. *Bull. Volcanol.* 58, 87–100.
- Kolzenburg, S., Heap, M., Lavallée, Y., Russell, J., Meredith, P., Dingwell, D.B., 2012. Strength and permeability recovery of tuffisite-bearing andesite. *Solid Earth* 3, 191.
- Kushnir, A.R., Martel, C., Bourdier, J.-L., Heap, M.J., Reuschlé, T., Erdmann, S., Komorowski, J.-C., Cholik, N., 2016. Probing permeability and microstructure: unravelling the role of a low-permeability dome on the explosivity of Merapi (Indonesia). *J. Volcanol. Geotherm. Res.* 316, 56–71.

- Kushnir, A.R., Martel, C., Champallier, R., Arbaret, L., 2017a. In situ confirmation of permeability development in shearing bubble-bearing melts and implications for volcanic outgassing. *Earth Planet. Sci. Lett.* 458, 315–326.
- Kushnir, A.R.L., Martel, C., Champallier, R., Wadsworth, F., 2017b. Permeability evolution in variably glassy basaltic andesites measured under magmatic conditions. *Geophys. Res. Lett.* 44.
- Lamur, A., Kendrick, J., Eggertsson, G., Wall, R., Ashworth, J., Lavallée, Y., 2017. The permeability of fractured rocks in pressurised volcanic and geothermal systems. *Sci. Rep.* 7, 6173.
- Lillis, R.J., Dufek, J., Kiefer, W.S., Black, B.A., Manga, M., Richardson, J.A., Bleacher, J.E., 2015. The Syrtis Major volcano, Mars: a multidisciplinary approach to interpreting its magmatic evolution and structural development. *J. Geophys. Res. Planets* 120, 1476–1496.
- McPhee, C.A., Arthur, K.G., 1991. Klinkenberg permeability measurements: problems and practical solutions. *Advances in Core Evaluation II: Reservoir Appraisal, Proceedings of the 2nd Society of Core Analysts European Core Analysis Symposium*. Gordon & Breach Science Publishers, Philadelphia, pp. 371–391.
- Melnik, O., Barmin, A., Sparks, R., 2005. Dynamics of magma flow inside volcanic conduits with bubble overpressure buildup and gas loss through permeable magma. *J. Volcanol. Geotherm. Res.* 143, 53–68.
- Michol, K., Russell, J., Andrews, G., 2008. Welded block and ash flow deposits from Mount Meager, British Columbia, Canada. *J. Volcanol. Geotherm. Res.* 169, 121–144. <https://doi.org/10.1016/j.jvolgeores.2007.08.010>.
- Mueller, S., Melnik, O., Spieler, O., Scheu, B., Dingwell, D.B., 2005. Permeability and degassing of dome lavas undergoing rapid decompression: an experimental determination. *Bull. Volcanol.* 67, 526–538.
- Nabovati, A., Llewellyn, E.W., Sousa, A.C., 2009. A general model for the permeability of fibrous porous media based on fluid flow simulations using the lattice Boltzmann method. *Compos. A: Appl. Sci. Manuf.* 40, 860–869. <https://doi.org/10.1016/j.compositesa.2009.04.009>.
- Nara, Y., Meredith, P.G., Yoneda, T., Kaneko, K., 2011. Influence of macro-fractures and micro-fractures on permeability and elastic wave velocities in basalt at elevated pressure. *Tectonophysics* 503, 52–59.
- Neuman, S.P., 1977. Theoretical derivation of Darcy's law. *Acta Mech.* 25, 153–170. <https://doi.org/10.1007/bf01376989>.
- Okumura, S., Nakamura, M., Takeuchi, S., Tsuchiyama, A., Nakano, T., Uesugi, K., 2009. Magma deformation may induce non-explosive volcanism via degassing through bubble networks. *Earth Planet. Sci. Lett.* 281, 267–274. <https://doi.org/10.1016/j.epsl.2009.02.036>.
- Okumura, S., Nakamura, M., Uesugi, K., Nakano, T., Fujioka, T., 2013. Coupled effect of magma degassing and rheology on silicic volcanism. *Earth Planet. Sci. Lett.* 362, 163–170.
- Papale, P., 1999. Strain-induced magma fragmentation in explosive eruptions. *Nature* 397, 425–428.
- Pickup, G., Stephen, K., Ma, J., Zhang, P., Clark, J., 2005. Multi-stage upscaling: selection of suitable methods. *Upscaling Multiphase Flow in Porous Media*. Springer, pp. 191–216.
- Pierson, T.C., Janda, R.J., Thouret, J.-C., Borrero, C.A., 1990. Perturbation and melting of snow and ice by the 13 November 1985 eruption of Nevado del Ruiz, Colombia, and consequent mobilization, flow and deposition of lahars. *J. Volcanol. Geotherm. Res.* 41, 17–66. [https://doi.org/10.1016/0377-0273\(90\)90082-q](https://doi.org/10.1016/0377-0273(90)90082-q).
- Piggott, A.R., Elsworth, D., 1992. Analytical models for flow through obstructed domains. *J. Geophys. Res. Solid Earth* 97, 2085–2093.
- Plail, M., Edmonds, M., Humphreys, M.C., Barclay, J., Herd, R.A., 2014. Geochemical evidence for relict degassing pathways preserved in andesite. *Earth Planet. Sci. Lett.* 386, 21–33.
- Renard, P., De Marsily, G., 1997. Calculating equivalent permeability: a review. *Adv. Water Resour.* 20, 253–278.
- Renard, P., Genty, A., Stauffer, F., 2001. Laboratory determination of full permeability tensor. *J. Geophys. Res.* 106, 26–443.
- Schauroth, J., Wadsworth, F.B., Kennedy, B., von Aulock, F.W., Lavallée, Y., Damby, D.E., Vasseur, J., Scheu, B., Dingwell, D.B., 2016. Conduit margin heating and deformation during the AD 1886 basaltic Plinian eruption at Tarawera volcano, New Zealand. *Bull. Volcanol.* 78, 12.
- Schumacher, R., Schmincke, H.U., 1990. The lateral facies of ignimbrites at Laacher See volcano. *Bull. Volcanol.* 52, 271–285. <https://doi.org/10.1007/bf00304099>.
- Smith, J., Miyake, Y., Oikawa, T., 2001. Interpretation of porosity in dacite lava domes as ductile-brittle failure textures. *J. Volcanol. Geotherm. Res.* 112, 25–35.
- Stinton, A.J., Cole, P.D., Stewart, R.C., Odber, H.M., Smith, P., 2014. The 11 February 2010 partial dome collapse at Soufrière Hills Volcano, Montserrat. *Geol. Soc. Lond. Mem.* 39, 133–152.
- Tidwell, V.C., 1996. Laboratory investigation of constitutive property up-scaling in volcanic tuffs. Technical Report. Sandia National Labs, Albuquerque, NM (United States).
- Tuffen, H., Dingwell, D., 2005. Fault textures in volcanic conduits: evidence for seismic trigger mechanisms during silicic eruptions. *Bull. Volcanol.* 67, 370–387.
- Varley, N.R., Taran, Y., 2003. Degassing processes of Popocatépetl and Volcán de Colima, Mexico. *Geol. Soc. Lond., Spec. Publ.* 213, 263–280. <https://doi.org/10.1144/gsl.sp.2003.213.01.16>.
- Venezky, D., Rutherford, M., 1997. Preeruption conditions and timing of dacite-andesite magma mixing in the 2.2 ka eruption at Mount Rainier. *J. Geophys. Res. Solid Earth* 102, 20069–20086.
- Vona, A., Romano, C., Dingwell, D., Giordano, D., 2011. The rheology of crystal-bearing basaltic magmas from Stromboli and Etna. *Geochim. Cosmochim. Acta* 75, 3214–3236.
- Wadsworth, F.B., Vasseur, J., Llewellyn, E.W., Dobson, K.J., Colombier, M., von Aulock, F.W., Fife, J.L., Wiesmaier, S., Hess, K.U., Scheu, B., et al. 2017. Topological inversions in coalescing granular media control fluid-flow regimes. *Phys. Rev. E* 96, 033113.
- Wadsworth, F.B., Vasseur, J., Scheu, B., Kendrick, J.E., Lavallée, Y., Dingwell, D.B., 2016. Universal scaling of fluid permeability during volcanic welding and sediment diagenesis. *Geology* 44, 219–222.
- Walker, G., Self, S., Froggett, P., 1981. The ground layer of the taupo ignimbrite: a striking example of sedimentation from a pyroclastic flow. *J. Volcanol. Geotherm. Res.* 10, 1–11. [https://doi.org/10.1016/0377-0273\(81\)90051-2](https://doi.org/10.1016/0377-0273(81)90051-2).
- Warren, J., Price, H., 1961. Flow in heterogeneous porous media. *Soc. Pet. Eng. J.* 1, 153–169.
- Watanabe, T., Shimizu, Y., Noguchi, S., Nakada, S., 2008. Permeability measurements on rock samples from Unzen Scientific Drilling Project drill hole 4 (USDP-4). *J. Volcanol. Geotherm. Res.* 175, 82–90.
- Westrich, H.R., Eichellberger, J.C., 1994. Gas transport and bubble collapse in rhyolitic magma: an experimental approach. *Bull. Volcanol.* 56, 447–458.
- Wilson, C.J.N., 1985. The Taupo Eruption, New Zealand II. The Taupo Ignimbrite. *Philos. Trans. R. Soc. A Math. Phys. Eng. Sci.* 314, 229–310. <https://doi.org/10.1098/rsta.1985.0020>.
- Wilson, C.J.N., Hildreth, W., 1997. The Bishop Tuff: new insights from eruptive stratigraphy. *J. Geol.* 105, 407–440. <https://doi.org/10.1086/515937>.
- Wright, H.M., Cashman, K.V., Gottesfeld, E.H., Roberts, J.J., 2009. Pore structure of volcanic clasts: measurements of permeability and electrical conductivity. *Earth Planet. Sci. Lett.* 280, 93–104. <https://doi.org/10.1016/j.epsl.2009.01.023>.
- Wright, H.M.N., Roberts, J.J., Cashman, K.V., 2006. Permeability of anisotropic tube pumice: model calculations and measurements. *Geophys. Res. Lett.* 33, <https://doi.org/10.1029/2006gl027224>.
- Zimmerman, R., Bodvarsson, G., 1996. Hydraulic conductivity of rock fractures. *Transp. Porous Media* 23, <https://doi.org/10.1007/bf00145263>.